

The lively accretion disk in NGC 2992. I. Transient iron K emission lines in the high flux state

A. Marinucci^{1*}, S. Bianchi², V. Braito^{3,4}, B. De Marco⁵, G. Matt², R. Middei^{6,7}, E. Nardini^{8,9}, J. N. Reeves^{3,4}

¹ASI - Unità di Ricerca Scientifica, Via del Politecnico snc, 00133, Roma, Italy

²Dipartimento di Matematica e Fisica, Università degli Studi Roma Tre, via della Vasca Navale 84, 00146 Roma, Italy

³Center for Space Science and Technology, University of Maryland Baltimore County, 1000 Hilltop Circle, Baltimore, MD 21250, USA

⁴INAF - Osservatorio Astronomico di Brera, Via Bianchi 46 I-23807 Merate (LC), Italy

⁵Nicolaus Copernicus Astronomical Center, Polish Academy of Sciences, Bartycka 18, PL-00-716 Warsaw, Poland

⁶INAF - Osservatorio Astronomico di Roma, Via Frascati 33, 00078, Monte Porzio Catone (Roma), Italy

⁷Space Science Data Center - ASI, Via del Politecnico s.n.c., 00133 Roma, Italy

⁸Dipartimento di Fisica e Astronomia, Università di Firenze, via G. Sansone 1, I-50019 Sesto Fiorentino, Firenze, Italy

⁹INAF - Osservatorio Astrofisico di Arcetri, Largo Enrico Fermi 5, 50125 Firenze, Italy

Accepted XXX. Received YYY; in original form ZZZ

ABSTRACT

We report on one of the brightest flux levels of the Seyfert 2 galaxy NGC 2992 ever observed in X-rays, on May 2019. The source has been monitored every few days from March 26, 2019 to December 14, 2019 by *Swift*-XRT, and simultaneous XMM-*Newton* (250 ks) and *NuSTAR* (120 ks) observations were triggered on May 6, 2019. The high count rate of the source (its 2–10 keV flux ranged between 0.7 and 1.0×10^{-10} erg cm⁻² s⁻¹) allows us to perform a time-resolved spectroscopy, probing spatial scales of tens of gravitational radii from the central black hole. By constructing a map of the excess emission over the primary continuum, we find several emission structures in the 5.0–7.2 keV energy band. From fitting the 50 EPIC pn spectral slices of ~ 5 ks duration, we interpret them as a constant narrow iron K α line and three variable components in the iron K complex. When a self-consistent model accounting for the accretion disk emission is considered (KYNRLINE), two of these features (in the 5.0–5.8 keV and 6.8–7.2 keV bands) can be ascribed to a flaring region of the accretion disk located at $r_{in} \simeq 15\text{--}40 r_g$ from the black hole. The third one (6.5–6.8 keV) is likely produced at much larger radii ($r_{in} > 50 r_g$). The inner radius and the azimuthal extension retrieved from the coadded spectra of the flaring states are $r_{in} = 15 \pm 3 r_g$ and $\phi = 165^\circ - 330^\circ$, suggesting that the emitting region responsible for the broad iron K component is a relatively compact annular sector within the disk. Our findings support a physical scenario in which the accretion disk in NGC 2992 becomes more active at high accretion rates ($L_{bol}/L_{Edd} \geq 4\%$).

Key words: Galaxies: active - Galaxies: Seyfert - Galaxies: accretion - Individual: NGC 2992

1 INTRODUCTION

Active Galactic Nuclei (AGN) that show high X-ray variability on relatively short (less than hundreds of ks) timescales are the perfect astrophysical laboratories for studying the response of the accretion disk to changes of the primary continuum. Spectral features both in emission and in absorption

have been detected in bright sources and can be studied to infer the physical properties of the circumnuclear matter (MCG-6-30-15, IRAS 13224-3809; Iwasawa et al. 1999; Fabian & Vaughan 2003; Marinucci et al. 2014; Parker et al. 2017b,a). On the other hand, the reverberation of the X-ray radiation reprocessed by the accretion disk (De Marco et al. 2013; Uttley et al. 2014; Kara et al. 2016) suggests that the hot corona, responsible for the primary continuum, has a typical size of a few gravitational radii and is located close

* E-mail: andrea.marinucci@asi.it (AM)

to the central supermassive black hole (SMBH). This is also supported by microlensing experiments on quasars (Chartas et al. 2009; Guerras et al. 2017).

A narrow neutral iron $K\alpha$ emission line at 6.4 keV is ubiquitous in nearby AGN (George et al. 2000; Perola et al. 2002; Bianchi et al. 2007) and when a broad component is detected, this is indicative of special and general relativistic effects (Nandra et al. 1997; Fabian et al. 2000; Reynolds & Nowak 2003) occurring at a few gravitational radii $r_g = GM/c^2$ from the central SMBH. Many studies on the variability pattern of such a broad iron $K\alpha$ component have been presented in the past (Iwasawa et al. 2004; Longinotti et al. 2004; Turner et al. 2006; Petrucci et al. 2007; Tombesi et al. 2007; De Marco et al. 2009; Nardini et al. 2016), typically on time scales of tens of ks.

NGC 2992 is a nearby ($z=0.00771$; Keel 1996) Seyfert 1.9/1.5 galaxy (Trippe et al. 2008). In X-rays, it is absorbed by a column density $N_H \sim 9 \times 10^{21} \text{ cm}^{-2}$ and it has been observed to vary in flux by up to a factor of 20 in a few years, and by almost an order of magnitude on time scales of days ($0.8\text{-}8.9 \times 10^{-11} \text{ erg cm}^{-2} \text{ s}^{-1}$; Murphy et al. 2007). Even though the source has been extensively observed by all major X-ray satellites, its high flux level is still poorly studied. The time variability of the iron $K\alpha$ line is intriguing, suggesting the presence of a broad iron $K\alpha$ component, between 5 and 6 keV, which becomes more intense at high flux levels (Yaqoob et al. 2007; Shu et al. 2010; Marinucci et al. 2018). This is the opposite of what is usually observed in other bright sources with relativistic lines and explained in the framework of the light bending model (Martocchia & Matt 1996; Miniutti & Fabian 2004).

We hereby present results from the XMM-Newton and NuSTAR observations of a high flux level of NGC 2992 occurred in May 2019 ($F_{2-10} > 7 \times 10^{-11} \text{ erg cm}^{-2} \text{ s}^{-1}$), with the aim of constraining the Fe K line emission regions, by monitoring the variability patterns of the line. The paper is structured as follows: in Sect. 2 we discuss the observations and data reduction, in Sect. 3 we present the iron K excess map, the excess variance F_{var} spectrum and the spectral analyses. We discuss and summarize the physical implications of our results in Sect. 4 and 5.

2 OBSERVATIONS AND DATA REDUCTION

2.1 Swift

The past RXTE ~ 1 year light curve (Murphy et al. 2007) showed a very broad range of 2-10 keV flux levels for NGC 2992 ($0.8\text{-}8.9 \times 10^{-11} \text{ erg cm}^{-2} \text{ s}^{-1}$). Our Swift-XRT monitoring program is composed of 60 observations, ~ 2 ks long each, from March 26, 2019 to December 14, 2019. The source was targeted every 2 days during the XMM-Newton observing windows and every 4 days in the remaining months. The requested high flux threshold ($F_{2-10} > 7 \times 10^{-11} \text{ erg cm}^{-2} \text{ s}^{-1}$) was met on May 6, 2019, with a 2-10 keV flux $F_{2-10} = 7.0 \pm 0.4 \times 10^{-11} \text{ erg cm}^{-2} \text{ s}^{-1}$. The complete Swift observational campaign will be analysed in a separate paper (Middei et al., in prep.).

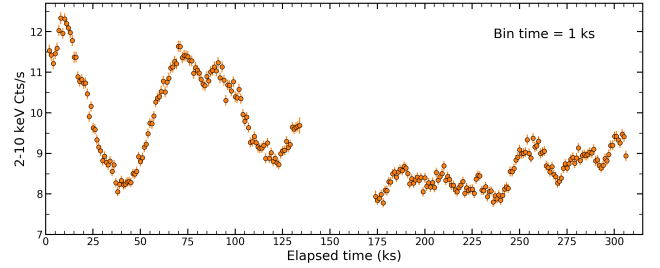


Figure 1. EPIC pn light curve of the two consecutive observations of NGC 2992, in the 2-10 keV energy band.

2.2 XMM-Newton

XMM-Newton started its observation of NGC 2992 on May 7, 2019 for two consecutive orbits (ObsIDs 0840920201, 0840920301) with the EPIC CCD cameras, the pn (Strüder et al. 2001) and the two MOS (Turner et al. 2001), operated in small window and medium filter mode. Data from the MOS detectors are not included in our analysis due to pile-up. The data from the pn camera show no significant pile-up as indicated by the EPATPLOT output. The extraction radii and the optimal time cuts for flaring particle background were computed with SAS 18 (Gabriel et al. 2004) via an iterative process which leads to a maximization of the Signal to Noise Ratio (SNR), similar to the approach described in Piconcelli et al. (2004). The resulting optimal extraction radii for the source and the background spectra are 40 and 50 arcsec, respectively. The net exposure times for the two time-averaged spectra are 92.6 and 92.8 ks. We then decided to extract spectra from 5.8 ks time intervals during the XMM-NuSTAR simultaneous observations (191-301 ks from the beginning of the XMM pointing) and from 5 ks time intervals when XMM data alone are available. This choice allows us to have a regular time spacing which is centered on the NuSTAR on-source pointing. With this choice, we obtained 26 and 24 spectra for the first and second XMM orbits, respectively. Spectra were then binned in order to over-sample the instrumental resolution by at least a factor of three and to have no less than 30 counts in each background-subtracted spectral channel, for the spectral fitting procedure. We adopt the cosmological parameters $H_0 = 70 \text{ km s}^{-1} \text{ Mpc}^{-1}$, $\Omega_\Lambda = 0.73$ and $\Omega_m = 0.27$, i.e. the default ones in XSPEC 12.10.1 (Arnaud 1996). Errors correspond to the 90% confidence level for one interesting parameter ($\Delta\chi^2 = 2.7$), if not stated otherwise.

2.3 NuSTAR

NuSTAR (Harrison et al. 2013) observed NGC 2992 with its two co-aligned X-ray telescopes with corresponding Focal Plane Module A (FPMA) and B (FPMB) on May 10, 2019 for a total of ~ 119.2 ks of elapsed time. The Level 1 data products were processed with the NuSTAR Data Analysis Software (NuSTARDAS) package (v. 1.8.0). Cleaned event files (level 2 data products) were produced and calibrated using standard filtering criteria with the NPIPELINE task and the latest calibration files available in the NuSTAR calibration database (CALDB 20190410). Extraction radii for the source and background spectra were 60 arcsec and 70

arcsec and the net exposure times for the two time-averaged spectra are 57.5 and 57.1 ks for the FPMA and FPMB, respectively. The two *NuSTAR* spectra were binned in order to over-sample the instrumental resolution by at least a factor of 2.5 and to have a SNR greater than 3σ in each spectral channel, for the spectral fitting procedure. We then adopted a linear time sampling of 5.8 ks, for a total number of 20 pairs of spectra. The cross-calibration factors between the two detectors were found to be within 2% in each time slice. A further constant was added (within 10% throughout the observation), to consider XMM-*NuSTAR* cross-calibration uncertainties.

3 DATA ANALYSIS

3.1 Estimates of the black hole mass

The EPIC pn light curves, extracted from the 2-10 keV energy band, are plotted in Fig. 1 and they show a count rate which ranges from 7.78 ± 0.11 to 12.33 ± 0.14 cts/s. They can be used to calculate a normalized excess variance $\sigma_{\text{rms}}^2 = 1.9 \pm 1.0 \times 10^{-3}$ (Nandra et al. 1997), adopting time bins of 250 s and selecting segments of 20 ks. Assuming the $\sigma_{\text{rms}}^2 - M_{\text{bh}}$ correlation reported in Ponti et al. (2012) we estimate a black hole mass $M_{\text{BH}} = (3.0^{+5.5}_{-1.5}) \times 10^7 M_{\odot}$, including also intrinsic uncertainties on the relation itself. The value obtained from the $M_{\text{BH}} - \sigma_{\star}$ relation is $M_{\text{BH}} = 4.8^{+3.9}_{-2.4} \times 10^7 M_{\odot}$, using a bulge stellar velocity dispersion $\sigma_{\star} = 158 \pm 13$ km/s (Nelson & Whittle 1995) and the relation from Gültekin et al. (2009). Given the good agreement between the M_{BH} inferred via the excess variance technique and the one derived from the $M_{\text{BH}} - \sigma_{\star}$ relation, we will use a value of $M_{\text{BH}} = 3.0^{+5.5}_{-1.5} \times 10^7 M_{\odot}$ for the black hole mass throughout the paper.

3.2 Time variability and excess maps

In the following, we will consider data in the 2-10 keV and 3-80 keV energy ranges for XMM and *NuSTAR* spectra. The detailed analysis of the broadband data set will be the subject of a different paper (Marinucci et al., in prep.). We first fitted the time-averaged spectra with a model composed of an absorbed power law (ZWABSXPOW in XSPEC) multiplied by a Galactic absorption component (TBABS) with $N_{\text{H}} = 4.8 \times 10^{20} \text{ cm}^{-2}$ (Kalberla et al. 2005), excluding the energy range dominated by the Fe K lines (5-8 keV). The ratios between the time-averaged data and the best fitting continuum models are plotted in Fig. 2, once the 5-8 keV band is included. A cross-calibration constant is added to the FPMA/B spectral fit and they are then simultaneously plotted using the SETPLOT GROUP command within XSPEC. The energy binning of the spectra is described in Sect. 2 and it is not the one used for creating the excess maps. Residuals are present on both the red and blue sides of the narrow iron $K\alpha$ emission line, in all the three data sets. The main spectral changes are in the 5-6 keV and 6.5-7.2 keV bands, with clear variations between the first and the second XMM orbit.

We then applied this model for the continuum to each of the 50 spectral slices. XMM and *NuSTAR* spectra are fitted simultaneously when simultaneous data are available

(time intervals between 191 ks and 301 ks), with the addition of a multiplicative constant to account for cross-calibration uncertainties. No residuals in excess to the best fit models are observed above 10 keV, suggesting a lack of a significant Compton hump due to cold reflection. Best fit models are stored and data with constant energy bins (100 eV for XMM and 200 eV for *NuSTAR*) are loaded. For each spectrum we calculate the the excess of counts with respect to the corresponding model and plot it as a function of energy and time. Any appreciable intensity variations are expected to occur on longer timescales than the sampling time (5-5.8 ks), therefore a smoothing procedure is expected to suppress the noise between adjacent pixels, providing a cleaner view of the possible variability patterns. Following the method described in Iwasawa et al. (2004) and Nardini et al. (2016) we smoothed the excess emission map through an elliptical Gaussian kernel with $(\sigma_{\text{E}}, \sigma_{\text{t}}) = (1.06, 1.27)$ pixels for the first XMM orbit and $(\sigma_{\text{E}}, \sigma_{\text{t}}) = (1.06, 1.10)$ for the second one: corresponding to a FWHM of $250 \text{ eV} \times 15 \text{ ks}$. The different width in time σ_{t} is due to the larger time intervals (5.8 ks rather than 5 ks) adopted in the second XMM orbit. FPMA/B detectors have a worse energy resolution (400 eV at 6 keV) than the EPIC pn and we used $(\sigma_{\text{E}}, \sigma_{\text{t}}) = (0.531, 1.10)$ pixels. For an energy binning of 200 eV and an integration time of 5.8 ks these values correspond to a FWHM of $250 \text{ eV} \times 15 \text{ ks}$. We plotted, in the four panels of Fig. 3, the energy-integrated count rates in excess to the continuum. We note that the energy bands of the smoothed data, due to the 250 eV width of the smoothing function, are wider than the ones used for the unsmoothed data. Counts integrated between 5 and 5.8 keV were associated to the *red flare*, between 6.2-6.5 keV to the narrow core of the iron $K\alpha$, between 6.5-6.8 keV to the *blue flare I* and between 6.8-7.2 keV to the *blue flare II*. The different energy bands, over-imposed to the time averaged spectra, can be seen in Fig. 2. Grey data points are used for plotting the excess count rates before the smoothing process in Fig. 3. We note that the smoothing process underestimates the 6.2-6.5 keV counts and overestimates the 6.5-6.8 keV counts (top panels in Fig. 3): this is an effect due to the 250 eV energy smoothing applied to the adjacent energy pixels. Assuming that the observed counts follow a Poissonian distribution ($\sigma_{\text{C}} = \sqrt{\text{C}}$), we calculated their error bars as the root sum of the squares of the errors extrapolated from the best fits of the continuum and the ones on the counts in excess. For comparison, we find 3282 ± 57 counts for the continuum and 171 ± 13 counts in excess in the 5-5.8 keV band, in the 10 ks spectral slice. During the second orbit, at 278 ks, we obtain 2803 ± 53 counts and 184 ± 14 counts for the continuum and for the excess, respectively. When we apply the smoothing filter, we lose the counting statistics and we therefore run extensive simulations to estimate the error on the plotted ratios, as detailed below. Following the procedures presented in Iwasawa et al. (2004) and De Marco et al. (2009), we simulated $N_{\text{sim}} = 1000$ time-energy maps with constant components in the four energy bands (obtained from fitting four Gaussians to the time-averaged spectra) with the associated best fit continuum model. Since the flux of the four spectral components (*red flare*, narrow iron $K\alpha$, *blue flare I* and *blue flare II*) is fixed in each simulation, the variance of the individual light curves after the smoothing serves as the measurement uncertainty. We therefore considered the mean variance of

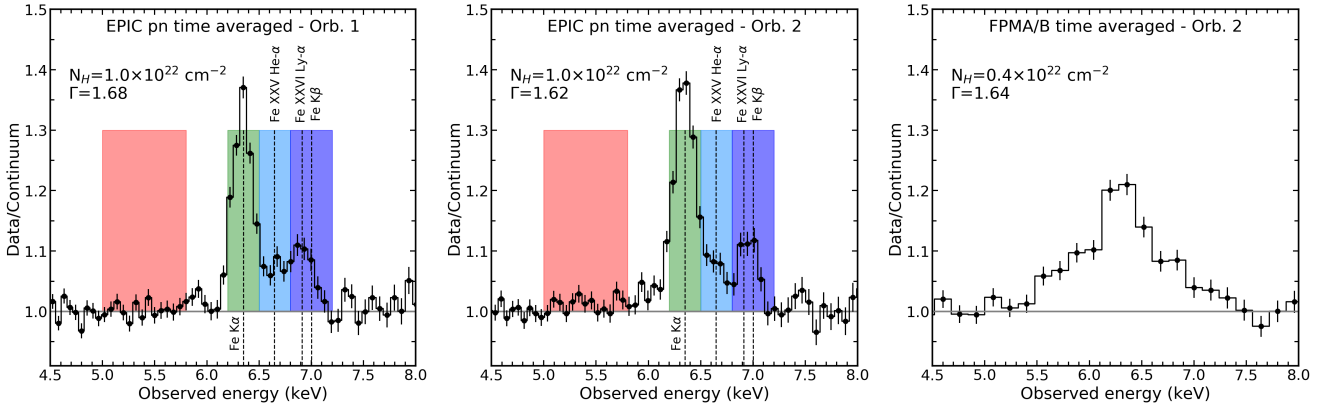


Figure 2. The ratios between the time-averaged data and the associated best fitting continuum models are shown, for the EPIC pn and FPMA/B observations. The continuum is composed of an absorbed power law fitted between 3-5 keV plus 8-10 keV, the best fitting values for the column density and photon index are reported in the top-left corner. The shaded regions indicate the four energy bands used for the variability patterns and the dashed lines show the emission lines between 6-7 keV included in the phenomenological spectral analysis.

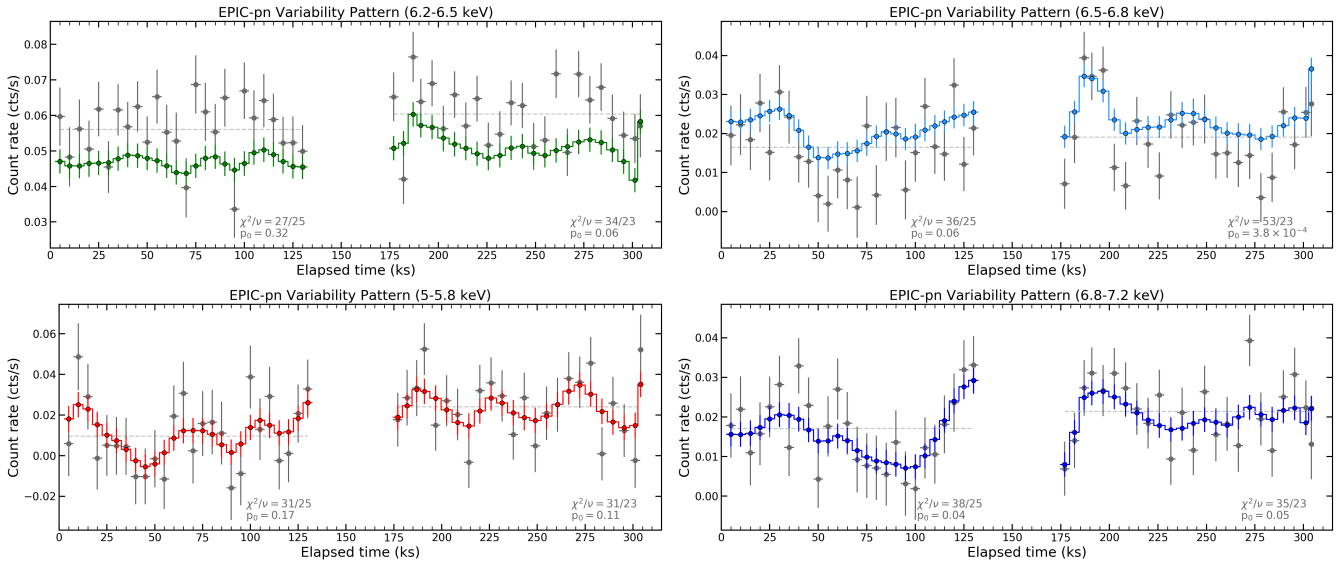


Figure 3. The smoothed excess count rates in the 6.2-6.5 keV, 6.5-6.8 keV, 5.0-5.8 keV, 6.8-7.2 keV bands are shown in green, light blue, red and dark blue, respectively. Unsmoothed data are shown in grey. The best fitting constant functions are shown as dashed grey lines.

the 1000 light curves and the standard deviation was assumed as the measurement error. To estimate the variability of the excess counts in the four energy bands we applied a constant model to the unsmoothed data points and the corresponding χ^2/ν values and null-hypothesis probabilities p_0 are reported in Fig. 3. The largest deviation from a constant model is observed for the *blue flare I* component, during the second orbit.

At last, we added two narrow Gaussian components to reproduce the constant iron $K\alpha/K\beta$ emission lines (with free energy and normalization for the former) to the XMM+*NuSTAR* continuum model and follow the previous steps to reproduce a count rate excess map. We will confirm in the next Section that this spectral components are statistically consistent with being constant throughout the

observation. The result is shown in Fig. 4. This is the first excess emission map constructed using *NuSTAR* data and, despite the lower spectral resolution and the non consecutive on-source spectra, a flux modulation in the 5.5-6.5 keV band can still be observed. However, for these two reasons, we will only consider XMM data hereinafter.

3.3 F_{var} spectrum

Following Vaughan et al. (2003), we computed the fractional root mean square (rms) variability amplitude (F_{var} : Ponti et al. 2004, 2006). To this aim we extracted light curves of each observation, in small energy bins (with a time bin of 50 s) and computed the Poisson-noise subtracted power spectrum (normalised to units of squared fractional rms,

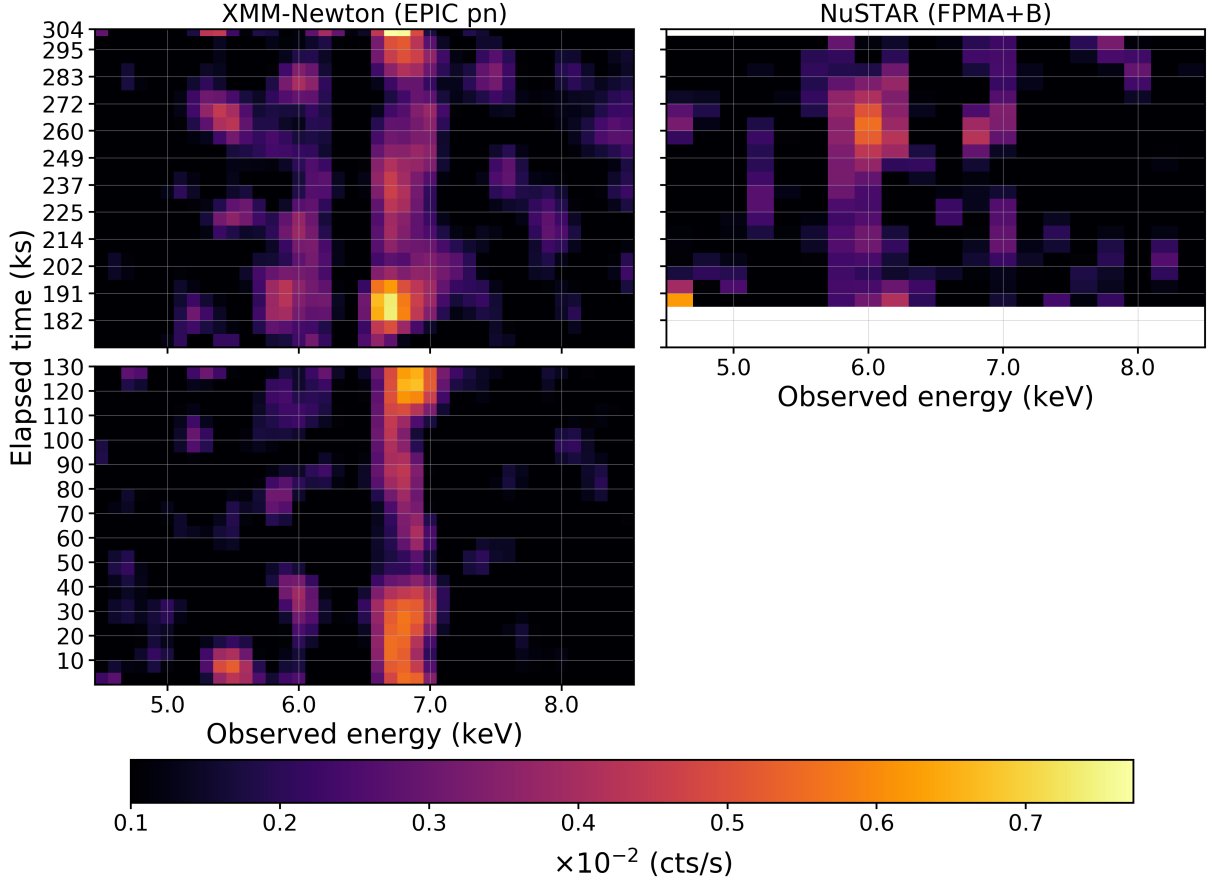


Figure 4. Excess emission map (in units of cts/s) for the full observation, when a model composed of a variable continuum and narrow iron $K\alpha/K\beta$ emission lines at 6.4 and 7.058 keV are considered.

Miyamoto et al. 1991). We integrated each power spectrum over the frequency range $0.9 \times 10^5 - 10^4$ Hz, corresponding to time scales ranging between 110 ks (approximately covering the entire duration of a single observation) and 10 ks. These time scales are chosen so as to sample the observed modulations in the Fe K line complex. From the square root of the integrated power we derived an estimate of the F_{var} as a function of energy, for each observation. Estimates from the two observations were then averaged to obtain the F_{var} spectrum displayed in Fig. 5. The F_{var} spectrum shows a spectral shape typical of absorbed sources (e.g. De Marco et al. 2020), with the soft energy drop due to the presence of constant spectral components which dominate this part of the spectrum. At higher energies (> 1 keV) the F_{var} increases ($\sim 7-9\%$), with a peak at ~ 2 keV and slightly decreasing towards harder energies. The sharp drop of F_{var} at $E \sim 6.4$ keV (marked by the vertical dashed line) is due to the presence of a constant neutral Fe $K\alpha$ emission line. At slightly lower energies ($E \sim 5-6$ keV) the F_{var} shows instead an increase, which hints at presence of enhanced variability associated with redshifted Fe K line components. This result is in agreement with the behavior observed in the excess map.

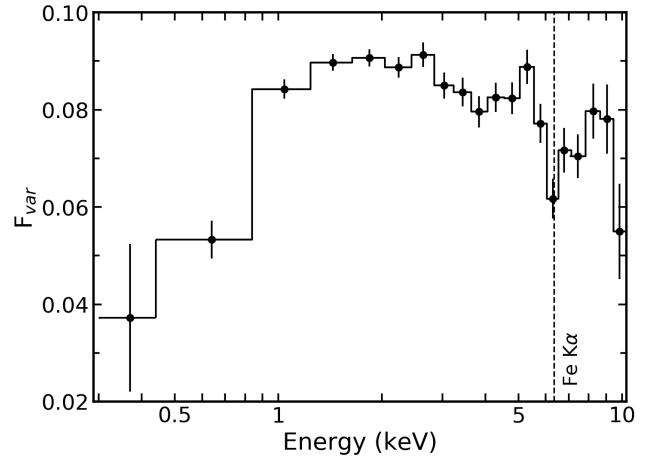


Figure 5. F_{var} spectrum of the full EPIC-pn observation. The dashed line indicates the neutral Fe $K\alpha$ observed energy.

3.4 Spectral fitting

In the following, we describe the 2-10 keV spectral fitting of the 50 EPIC pn spectra. Our aim is to characterize and explain the observed variability patterns around the Fe K complex, using both a phenomenological and a self-consistent

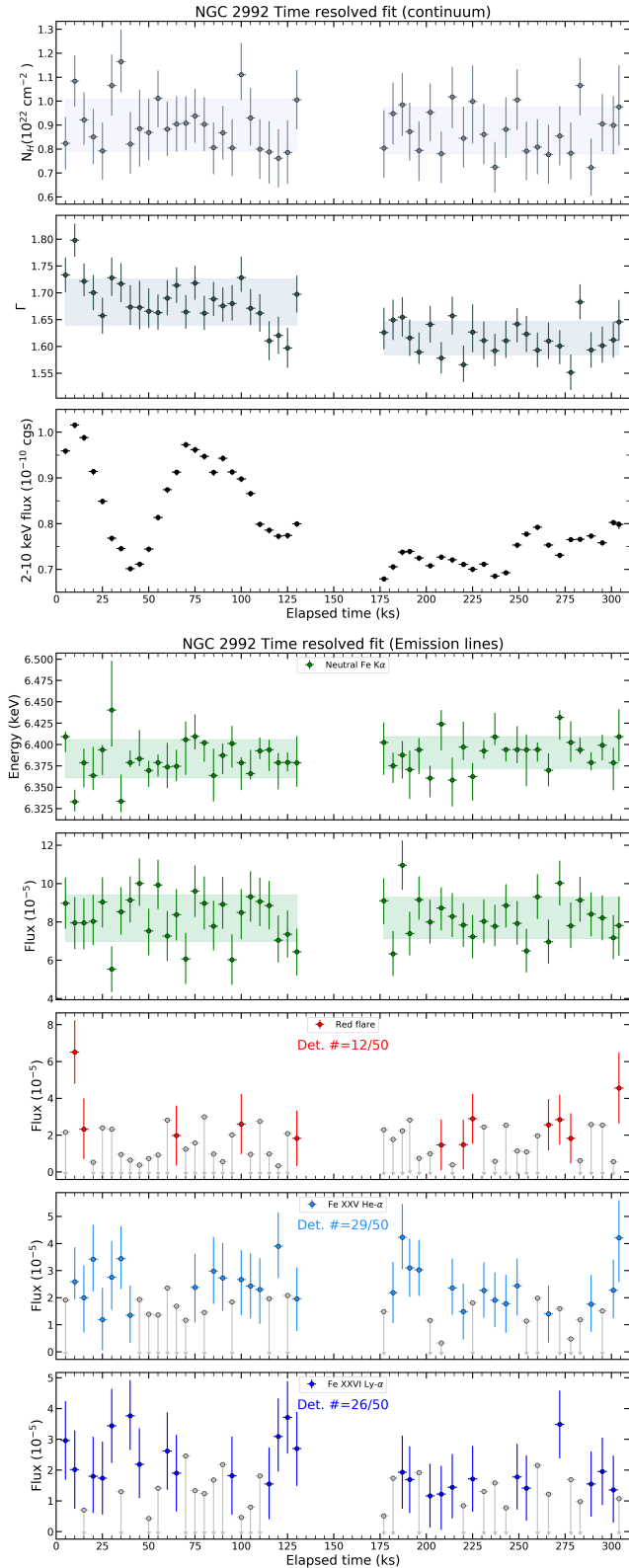


Figure 6. Best fit values for the continuum (top-panels) and emission lines (bottom-panels) when the phenomenological model described in Sect. 3.3.1 is applied to the XMM data set. Fluxes are in $\text{ph cm}^{-2} \text{s}^{-1}$ units and shaded regions indicate 1σ above and below mean values. Errors are calculated using 68% c.l. The number of intervals in which the emission lines are detected is reported in the top center of bottom panels.

physical model. We first model the counts excesses in the four energy bands shown in Fig. 3 with variable Gaussians and then with flaring spots from the accretion disk.

3.4.1 Phenomenological analysis

The phenomenological model applied to the data set is composed of the absorbed power law considered in Sect. 3.1 and five narrow Gaussian lines, to reproduce the neutral Fe $K\alpha$ and $K\beta$, the Fe xxv He- α and the Fe xxvi Ly- α emission lines at 6.4 keV, 7.058 keV, 6.7 keV and 6.966 keV, respectively. One additional Gaussian is included in the model to reproduce the *red flare*. The normalization of the Fe $K\beta$ line is fixed to $0.16 \times N_{K\alpha}$ (Molendi et al. 2003). The free parameters in the fits are the column density N_{H} , the photon index Γ , the energy centroid of the neutral Fe $K\alpha$ and the normalization of the power law and of the four emission lines. The energy centroid of the spectral component associated to the *red flare* is fixed to 5.4 keV. We show the best fitting values in Fig. 6, errors are calculated using a 68 % confidence level. The shaded regions indicate 1σ above and below the mean N_{H} , Γ , energy centroid and flux of the neutral iron $K\alpha$. The number of detected emission lines is reported in the top-center of the three bottom panels. The minimum and maximum flux levels measured throughout the observation are $F_{2-10} = (6.8 \pm 0.1) \times 10^{-11} \text{ erg cm}^{-2} \text{ s}^{-1}$ and $F_{2-10} = (1.01 \pm 0.01) \times 10^{-10} \text{ erg cm}^{-2} \text{ s}^{-1}$, corresponding to luminosities $L_{2-10} = 9.5 \times 10^{42} \text{ erg s}^{-1}$ and $L_{2-10} = 1.5 \times 10^{43} \text{ erg s}^{-1}$ (corrected for intrinsic absorption), respectively. Adopting the bolometric correction $K_X(L_X)$ from Duras et al. (2020) and a black hole mass $M_{\text{BH}} = 3 \times 10^7 M_{\odot}$, we obtain an accretion rate interval $L_{\text{Bol}}/L_{\text{Edd}} \approx 4\text{-}6\%$.

While the neutral Fe $K\alpha$ normalization is statistically consistent with being constant throughout the observation, variations of the other emission lines are detected. The maxima of the *red flare* normalization occur at 10 ks and 304 ks. For the sake of a visual comparison, we plot in the top panel of Fig. 7 the ratio between the data and the absorbed power law model for the time averaged spectrum (185.5 ks long) and for the two spectral slices corresponding to 10 ks and 50 ks, in which the maximum and an upper limit are retrieved for the *red flare* component. We show in the bottom panel of Fig. 7 the same ratios but for the maximum of the *blue flare I* component. The maxima of the Fe xxv He- α and Fe xxvi Ly- α components occur at 187 ks and 40 ks, respectively. These values are in perfect agreement with our results from the excess map technique (Fig. 3 and Fig. 4). The timescales of the detected variations of the four phenomenological emission lines are consistent with distances of $\sim 30\text{-}40 r_g$ (for light-crossing times of 5-6 ks). This motivates the usage of a self-consistent model in which the transient Fe K lines are due to various orbiting flaring regions above the accretion disk.

3.4.2 The KYNRLINE model

In this Section, we apply the KYN model (Dovčiak et al. 2004) to the 50 EPIC pn spectra. The change of the emission lines amplitude and energy is explained in terms of orbital motion in a relativistic gravitational field close to the

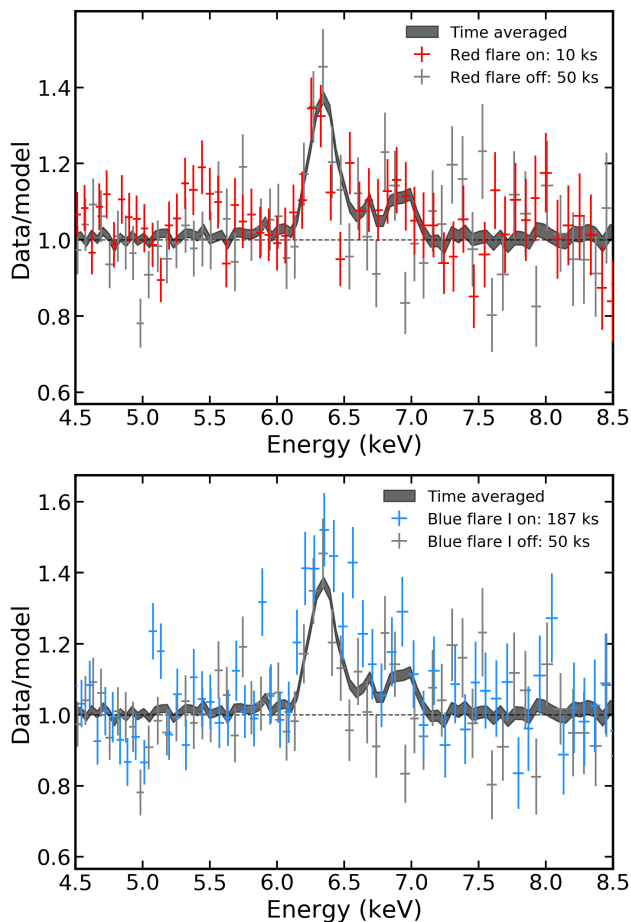


Figure 7. The ratios between the data and the absorbed power law model is shown for the time averaged spectrum (black shaded region) and for the two spectral slices corresponding to 10 ks (red data points, top panel), 187 ks (light blue data points, bottom panel) and 50 ks (grey data points), which are representative of the two flaring and one quiescent state.

central black hole. The model assumes a space-time around the black hole which is described by the Kerr metric and a Keplerian, geometrically thin and optically thick accretion disk¹. In particular, we use the KYNRLINE model component in XSPEC, which reproduces a relativistic line with a broken power-law radial emissivity. The emitting regions are non-axisymmetric, i.e. only part of the disc may be emitting (sections in radius and azimuth).

We first adopt a model which is composed of the absorbed power law considered in Sect. 3.1 and two narrow Gaussian lines, to reproduce the neutral Fe $K\alpha$ and $K\beta$. The parameters Γ , N_{H} and normalization of the continuum are free. The Fe $K\beta$ is always included in the following fits and its normalization is fixed to $0.16 \times N_{K\alpha}$. The neutral Fe $K\alpha$ energy centroid and normalization are free. We then included a KYNRLINE component, fixing the emissivity of the disk to $\epsilon(r) \propto r^{-3}$, the black hole spin to $a^* = 0.998$ and the annular region extension to $10 r_g$. In our fits, we chose

¹ a full description of the model can be found at <https://projects.asu.cas.cz/stronggravity/kyn/>

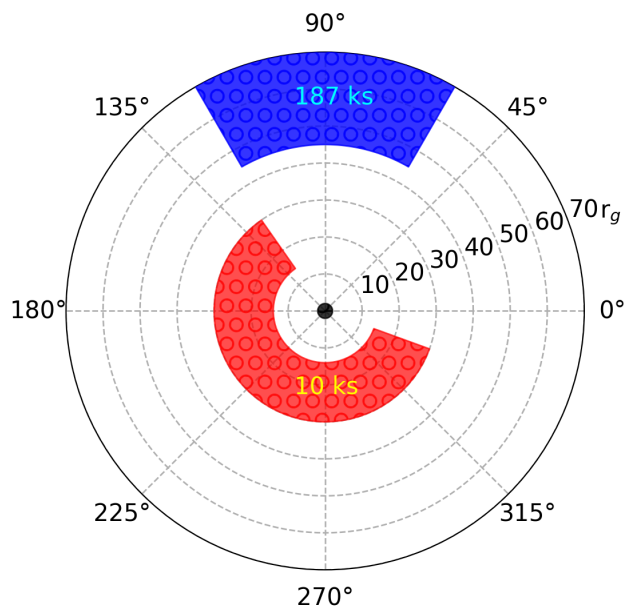


Figure 8. Schematic view of the emitting regions associated to the two KYNRLINE components described in Sect. 3.3.2. The red area indicates the best fitting values which reproduce the *red flare* and the *blue flare II* at 10 ks, when the 5–5.8 keV excess is maximum. The blue one shows the best fitting values for the *blue flare I* at its maximum, during the 187 ks time interval.

a framework where positive angular velocity corresponds to counterclockwise rotation and $\phi = 0^\circ, 360^\circ$ to the maximal Doppler blueshift for matter moving toward the observer (same convention as in Dovčiak et al. 2004; Nardini et al. 2016). We also assumed an energy at rest $E_{\text{R}} = 6.7$ keV and an inclination angle of the accretion disk $i = 40^\circ$ with respect to our line of sight (Yaqoob et al. 2007). The properties of the emitting annuli are therefore estimated by leaving the inner radius r_{in} , the angle ϕ and the angular extension $\Delta\phi$ free in the fits. For simplicity, the reported uncertainties on the angular sizes are the lower errors on ϕ and the upper errors on $\Delta\phi$. This first KYNRLINE spectral component reproduces the 5.4 keV and the 7.0 keV observed peaks (*red flare + blue flare II*). A second KYNRLINE component is then included in the model to account for the 6.7 keV excess (*blue flare I*).

This model is applied to the 50 EPIC pn spectral slices. Best fit values for the primary continuum, neutral Fe $K\alpha$ line, annular extension, size and normalization of the KYNRLINE components are reported in Table 1. All the spectra, the corresponding best fit models and the relative residuals, are shown in Fig. A1 and A2. We plot in Fig. 8 a sketch of the emitting regions associated to the two KYNRLINE components for the 10 ks and 187 ks time intervals.

4 DISCUSSION

The EPIC-pn time variability patterns presented in Sect. 3.2 have shown several transient emission features throughout the 5–7 keV band and some recursive flares in the 5–5.8 keV band can be seen in Fig. 3 and 4. If a sinusoidal function is

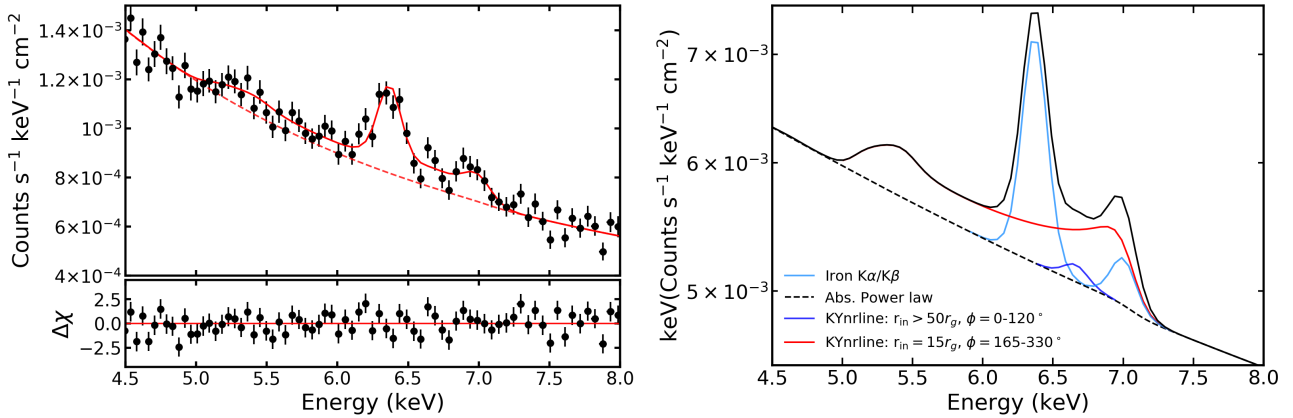


Figure 9. *Left panel:* the *flaring mode* spectrum and the best fitting model are plotted with the corresponding residuals. The spectrum is the sum of the ones extracted from time intervals peaking at 191, 225, 272 and 304 ks. *Right panel:* the final KYNRLINE model applied to the 50 EPIC pn spectra is shown in black, in the 4.5-8 keV band only. This represents the best fitting model of the *flaring mode* spectrum only, the different components are free in each spectral slice. The dashed black line indicates the absorbed power law component and the narrow iron $K\alpha$ and $K\beta$ emission lines are plotted in cyan. We show the *red flare + blue flare II* ($r_{\text{in}} = 15 \pm 3 r_g$, $\phi = 165^\circ - 330^\circ$) and *blue flare I* ($r_{\text{in}} > 50 r_g$, $\phi = 0^\circ - 120^\circ$) components as red and blue solid lines, respectively.

applied to the unsmoothed data of the second XMM orbit (Fig. 3, bottom-left panel) a best fitting orbital period $T = 41 \pm 1$ ks is retrieved, with a corresponding $\chi^2/\nu = 20/20$. Assuming a maximally rotating black hole spin and a black hole mass $M_{\text{BH}} = 3.0^{+5.5}_{-1.5} \times 10^7 M_\odot$, we can use the relation from Bardeen et al. (1972) to estimate the radial distance r from the inferred orbital period T :

$$T = 310 \left[a + \left(\frac{r}{r_g} \right)^{\frac{3}{2}} \right] M_7 \text{ (s)}, \quad (1)$$

$$r = \left[\frac{T}{310 \times M_7} - a \right]^{\frac{2}{3}} r_g = 12^{+8}_{-6} r_g,$$

where M_7 is the black hole mass in $10^7 M_\odot$ units and a is the dimensionless back hole spin. The error bars on the radial distance r are dominated by the uncertainties on the black hole mass. We note, however, that Vaughan & Uttley (2008) observed that the detection of relativistically redshifted iron K lines could be the result of random fluctuations and Vaughan et al. (2016) estimated that at least five periodicities should be sampled to exclude a stochastic process effect.

To enhance the significance of the transient iron K lines, we co-added data extracted from time intervals with similar parameters of the continuum (i.e. column density, 2-10 keV flux and photon index) and in which the flares are most significant. We chose the time intervals peaking at 191, 225, 272, 304 ks, for a total exposure time of 14.6 ks. We will call this co-added spectrum *flaring mode* spectrum (Fig. 9, left panel).

When the KYNRLINE model described in the previous section is applied to the *flaring mode* spectrum we retrieve a best fit $\chi^2/\nu = 135/137$, a best fitting energy at rest $E_R = 6.7 \pm 0.1$ keV and an inclination angle of the accretion disk $i = 40^\circ \pm 5^\circ$ with respect to our line of sight, justifying our previous assumptions on these two parameters. The best fitting values for the KYNRLINE component reproducing the *red flare* and *blue flare II* are $r_{\text{in}} = 15 \pm 3 r_g$, $\phi = 165^\circ - 330^\circ$ and $N = 11.5 \pm 3.5 \times 10^{-5}$ ph $\text{cm}^{-2} \text{s}^{-1}$. This spectral compo-

nent well reproduces the 5.4 keV and 7.0 keV peaks and its very broad shape (red solid line in the right-panel of Fig. 9) is explained in terms of an emitting region close to a full ring of the accretion disk. The second KYNRLINE component (blue solid line in the right-panel of Fig. 9) is much narrower than the first one and the associated parameters are $r_{\text{in}} > 50 r_g$, $\phi = 0^\circ - 120^\circ$ and $N = 4.5 \pm 4.0 \times 10^{-6}$ ph $\text{cm}^{-2} \text{s}^{-1}$. The total best fitting model is shown in Fig. 9 as a black solid line.

We show in Fig. 10 the contour plots between r_{in} and the normalization: a perfect agreement between r_{in} and the radial distance r retrieved from the periodicity of the *red flare* can be seen. Furthermore, the best fit values for the inclination angle of the accretion disk, the inner radius and the normalization of the *red flare + blue flare II* component are perfectly consistent with the ones derived from previous high flux *RXTE* and XMM observations (Murphy et al. 2007; Shu et al. 2010).

5 CONCLUSIONS

In the previous sections, we presented the analysis of the first simultaneous XMM+*NuSTAR* observations of NGC 2992 in an extremely bright state. The source is known to be intrinsically variable, up to a factor of 10 on timescales of days, as observed during the past *RXTE* monitoring (Murphy et al. 2007). It was observed multiple times by XMM-*Newton* between 2010 and 2013, with a 2-10 keV flux always lower than $F_{2-10} < 1.7 \times 10^{-11}$ erg $\text{cm}^{-2} \text{s}^{-1}$. The only XMM observation of the source in the 2003 bright state was heavily affected by pile-up (Shu et al. 2010). Nevertheless, the authors found a relativistic iron $K\alpha$, in accordance with what already observed with *RXTE*. To tackle the high flux levels of the source (i.e. $F_{2-10} > 7 \times 10^{-11}$ erg $\text{cm}^{-2} \text{s}^{-1}$), we obtained 60 *Swift*-XRT snapshots from March 26, 2019 to December 14, 2019 and the triggered XMM-*NuSTAR* observations started on May 7, 2019. We observe a range of fluxes corresponding to accretion rates

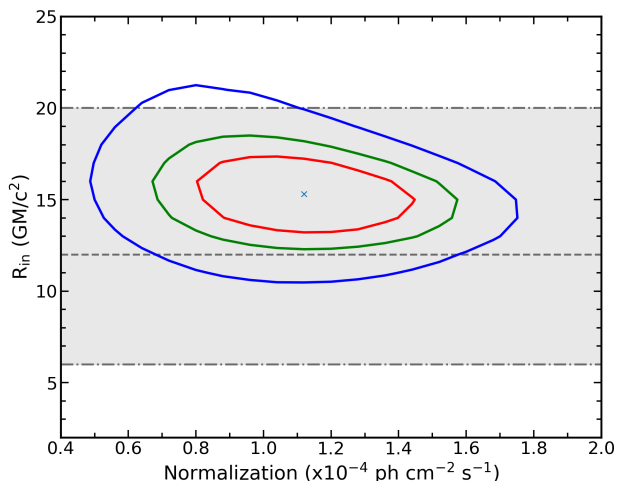


Figure 10. Contour plots between the inner radius of the annular region and the normalization of the *red flare* + *blue flare II* KYNRLINE component are shown, obtained from the best fit of the co-added spectra of NGC 2992 in the flaring state. Red, green and blue solid lines indicate 68%, 90% and 99% confidence levels. The dashed and dotted-dashed black lines indicate the radial distance with its associated errors obtained from the periodicity of the *red flare* (see Sect. 3.2 for details).

$L_{\text{Bol}}/L_{\text{Edd}} \approx 4\text{--}6\%$ and we confirm the physical scenario in which the source exhibits strong redshifted/blueshifted Fe K lines at $L_{\text{Bol}}/L_{\text{Edd}} > 4\%$ (Murphy et al. 2007; Marinucci et al. 2018).

From the XMM-Newton excess emission map shown in Sect. 3.2, we find hints of a recursive *red flare* at ~ 5.4 keV, with a period $T = 41 \pm 1$ ks. For a maximally rotating black hole spin and considering the black hole mass of the source, the inferred period corresponds to a radial distance $r = 12^{+8}_{-6} r_g$. A fully consistent value is found when the KYNRLINE model is applied to the co-added spectra of the flaring states only ($r_{\text{in}} = 15 \pm 3 r_g$). We find that the *red flare* is likely associated to a second spectral component (*blue flare II*, at ~ 7.0 keV) and can be modelled with a line-emitting annular region close to a full ring of the disk.

In the last few years, the technique of mapping the time variability of the flux in excess to the continuum, at different energies, has led to a number of results in bright AGN, with NGC 3516 (Iwasawa et al. 2004), Mrk 766 (Turner et al. 2006), NGC 3783 (Tombesi et al. 2007) and Ark 120 (Nardini et al. 2016) being the most significant ones. Differently from NGC 3516 and Mrk 766, we cannot constrain a clear evolution of the energy centroid of the emission lines, only changes in fluxes are detected. In our model, the *red flare* + *blue flare II* component likely arises from large angular regions close to the central black hole ($\phi \approx 150^\circ - 360^\circ$, $r_{\text{in}} \approx 10 - 40 r_g$), and well reproduces the excesses observed at 5–5.8 keV and 6.8–7.2 keV. The width of this sector is not due to the limited spectral quality of our data, but mainly by the necessity to account for both the red and most of the blue excess. On the other hand, the *blue flare I* component is much narrower and it is consistent with arising from smaller angular sectors, further away in the disk ($\phi \approx 0^\circ - 150^\circ$, $r_{\text{in}} > 50 r_g$). The hotspot scenario (Ruszkowski 2000; Nayakshin & Kazanas

2001; Dovčiak et al. 2004) is often invoked to explain the observed variability of narrow iron K α emission lines, both in energy and in flux. However, due to the lack of a significant shift in energy of the emission features observed and due to the large angular sectors which best reproduce the red component modulation, the hotspot picture seems unlikely. A single orbital spot cannot reproduce the whole variability patterns and the scenario seems much more complex. In particular, the periodicity of the *red flare* which is not observed in the *blue flare II* (bottom panels of Fig. 3) suggests that their angular distance cannot be resolved and only part of the angular sector is responsible for the periodical excess. Future X-ray observatories with higher spectral resolution and much larger effective area (such as *Athena*, *eXTP*, *XRISM*) will be crucial for this kind of studies.

ACKNOWLEDGEMENTS

We thank the anonymous referee for her/his suggestions which improved the manuscript. AM thanks A. De Rosa and M. Dovčiak for useful discussions. AM and RM acknowledge the support of the International Space Science Institute (ISSI Bern, Switzerland). BDM acknowledges support from the European Union’s Horizon 2020 research and innovation programme under the Marie Skłodowska-Curie grant agreement No. 798726 and Polish National Science Center grant OPUS No. 2015/17/B/ST9/03422. We made use of ASTROPY,² a community-developed core PYTHON package for Astronomy (Astropy Collaboration et al. 2013, 2018) and MATPLOTLIB (Hunter 2007). This research has made use of the NuSTAR Data Analysis Software (NuSTARDAS) jointly developed by the ASI Science Data Center (ASDC, Italy) and the California Institute of Technology (USA).

REFERENCES

- Arnaud K. A., 1996, in ASP Conf. Ser. 101: Astronomical Data Analysis Software and Systems V. p. 17
- Astropy Collaboration et al., 2013, *A&A*, **558**, A33
- Astropy Collaboration et al., 2018, *AJ*, **156**, 123
- Bardeen J. M., Press W. H., Teukolsky S. A., 1972, *ApJ*, **178**, 347
- Bianchi S., Guainazzi M., Matt G., Fonseca Bonilla N., 2007, *A&A*, **467**, L19
- Chartas G., Kochanek C. S., Dai X., Poindexter S., Garmire G., 2009, *ApJ*, **693**, 174
- De Marco B., Iwasawa K., Cappi M., Dadina M., Tombesi F., Ponti G., Celotti A., Miniutti G., 2009, *A&A*, **507**, 159
- De Marco B., Ponti G., Cappi M., Dadina M., Uttley P., Cackett E. M., Fabian A. C., Miniutti G., 2013, *MNRAS*, **431**, 2441
- De Marco B., et al., 2020, *A&A*, **634**, A65
- Dovčiak M., Bianchi S., Guainazzi M., Karas V., Matt G., 2004, *MNRAS*, **350**, 745
- Duras F., et al., 2020, arXiv e-prints, p. arXiv:2001.09984
- Fabian A. C., Vaughan S., 2003, *MNRAS*, **340**, L28
- Fabian A. C., Iwasawa K., Reynolds C. S., Young A. J., 2000, *PASP*, **112**, 1145

² <http://www.astropy.org>

Gabriel C., et al., 2004, in F. Ochsenbein, M. G. Allen, & D. Egret ed., *Astronomical Society of the Pacific Conference Series* Vol. 314, *Astronomical Data Analysis Software and Systems (ADASS) XIII*. pp 759–+

George I. M., Turner T. J., Yaqoob T., Netzer H., Laor A., Mushotzky R. F., Nandra K., Takahashi T., 2000, *ApJ*, **531**, 52

Guerras E., Dai X., Steele S., Liu A., Kochanek C. S., Chartas G., Morgan C. W., Chen B., 2017, *ApJ*, **836**, 206

Gültekin K., et al., 2009, *ApJ*, **698**, 198

Hunter J. D., 2007, *Computing in Science & Engineering*, 9, 90

Iwasawa K., Fabian A. C., Young A. J., Inoue H., Matsumoto C., 1999, *MNRAS*, **306**, L19

Iwasawa K., Miniutti G., Fabian A. C., 2004, *MNRAS*, **355**, 1073

Kalberla P. M. W., Burton W. B., Hartmann D., Arnal E. M., Bajaja E., Morras R., Pöppel W. G. L., 2005, *A&A*, **440**, 775

Kara E., Alston W. N., Fabian A. C., Cackett E. M., Uttley P., Reynolds C. S., Zoghbi A., 2016, *MNRAS*, **462**, 511

Keel W. C., 1996, *ApJS*, **106**, 27

Longinotti A. L., Nandra K., Petrucci P. O., O’Neill P. M., 2004, *MNRAS*, **355**, 929

Marinucci A., et al., 2014, *ApJ*, **787**, 83

Marinucci A., Bianchi S., Braitto V., Matt G., Nardini E., Reeves J., 2018, *MNRAS*, **478**, 5638

Martocchia A., Matt G., 1996, *MNRAS*, **282**, L53

Miniutti G., Fabian A. C., 2004, *MNRAS*, **349**, 1435

Miyamoto S., Kimura K., Kitamoto S., Dotani T., Ebisawa K., 1991, *ApJ*, **383**, 784

Molendi S., Bianchi S., Matt G., 2003, *MNRAS*, **343**, L1

Murphy K. D., Yaqoob T., Terashima Y., 2007, *ApJ*, **666**, 96

Nandra K., George I. M., Mushotzky R. F., Turner T. J., Yaqoob T., 1997, *ApJ*, **477**, 602

Nardini E., Porquet D., Reeves J. N., Braitto V., Lobban A., Matt G., 2016, *ApJ*, **832**, 45

Nayakshin S., Kazanas D., 2001, *ApJ*, **553**, L141

Nelson C. H., Whittle M., 1995, *ApJS*, **99**, 67

Parker M. L., et al., 2017a, *MNRAS*, **469**, 1553

Parker M. L., et al., 2017b, *Nature*, **543**, 83

Perola G. C., Matt G., Cappi M., Fiore F., Guainazzi M., Maraschi L., Petrucci P. O., Piro L., 2002, *A&A*, **389**, 802

Petrucci P. O., et al., 2007, *A&A*, **470**, 889

Piconcelli E., Jimenez-Bailón E., Guainazzi M., Schartel N., Rodríguez-Pascual P. M., Santos-Lleó M., 2004, *MNRAS*, **351**, 161

Ponti G., Cappi M., Dadina M., Malaguti G., 2004, *A&A*, **417**, 451

Ponti G., Miniutti G., Cappi M., Maraschi L., Fabian A. C., Iwasawa K., 2006, *MNRAS*, **368**, 903

Ponti G., Papadakis I., Bianchi S., Guainazzi M., Matt G., Uttley P., Bonilla N. F., 2012, *A&A*, **542**, A83

Reynolds C. S., Nowak M. A., 2003, *Phys. Rep.*, **377**, 389

Ruszkowski M., 2000, *MNRAS*, **315**, 1

Shu X. W., Yaqoob T., Murphy K. D., Braitto V., Wang J. X., Zheng W., 2010, *ApJ*, **713**, 1256

Strüder L., et al., 2001, *A&A*, **365**, L18

Tombesi F., De Marco B., Iwasawa K., Cappi M., Dadina M., Ponti G., Miniutti G., Palumbo G. G. C., 2007, *A&A*, **467**, 1057

Trippé M. L., Crenshaw D. M., Deo R., Dietrich M., 2008, *AJ*, **135**, 2048

Turner M. J. L., et al., 2001, *A&A*, **365**, L27

Turner T. J., Miller L., George I. M., Reeves J. N., 2006, *A&A*, **445**, 59

Uttley P., Cackett E. M., Fabian A. C., Kara E., Wilkins D. R., 2014, *A&ARv*, **22**, 72

Vaughan S., Uttley P., 2008, *MNRAS*, **390**, 421

Vaughan S., Edelson R., Warwick R. S., Uttley P., 2003, *MNRAS*, **345**, 1271

Vaughan S., Uttley P., Markowitz A. G., Huppenkothen D., Middleton M. J., Alston W. N., Scargle J. D., Farr W. M., 2016, *MNRAS*, **461**, 3145

Yaqoob T., et al., 2007, *PASJ*, **59**, 283

APPENDIX A: BEST FIT RESULTS WITH KYNRLINE

We present in Table A1 the best fit parameters obtained with the KYNRLINE model described in Sect. 3.4.2. We show in Fig. A1 and A2 the spectra, the corresponding best fit models and the relative residuals from the full XMM-Newton observation.

This paper has been typeset from a $\text{\TeX}/\text{\LaTeX}$ file prepared by the author.

Time	Best fit parameter										χ^2/ν
	N_{H} ($\times 10^{22}$)	Γ	$E_{\text{K}\alpha}$	$N_{\text{K}\alpha}$ ($\times 10^{-5}$)	Red flare + Blue flare II			Blue flare I			
					r_{in}	ϕ	N_{RS} ($\times 10^{-5}$)	r_{in}	ϕ	N_{BS} ($\times 10^{-5}$)	
Orbit 1											
5 ks	0.82 ± 0.18	1.74 ± 0.05	6.41 ± 0.03	8.1 ± 2.2	20^{+40}_{-10}	180^{+160}_{-20}	9.0 ± 6.2	-	-	<1.7	114/113
10 ks	1.08 ± 0.18	1.80 ± 0.05	$6.34^{+0.04}_{-0.01}$	6.3 ± 2.3	17 ± 3	140^{+200}_{-15}	14.7 ± 3.0	-	-	<2.8	116/115
15 ks	0.93 ± 0.20	1.72 ± 0.05	6.38 ± 0.04	7.7 ± 2.3	-	-	<7.1	-	-	<3.9	126/117
20 ks	0.82 ± 0.20	1.70 ± 0.05	$6.37^{+0.05}_{-0.03}$	7.0 ± 2.0	25^{+15}_{-5}	175^{+170}_{-20}	9.2 ± 6.3	-	-	<4.5	122/112
25 ks	0.78 ± 0.19	1.65 ± 0.05	6.38 ± 0.02	9.0 ± 2.5	-	-	<6.7	-	-	<3.2	103/118
30 ks	1.07 ± 0.21	1.74 ± 0.05	$6.37^{+0.06}_{-0.07}$	2.8 ± 2.8	45^{+20}_{-10}	180^{+190}_{-15}	10.7 ± 5.5	>80	100^{+20}_{-30}	2.8 ± 2.1	134/123
35 ks	1.11 ± 0.23	1.71 ± 0.06	6.31 ± 0.07	5.5 ± 2.5	-	-	<7.0	30^{+30}_{-10}	60^{+80}_{-15}	8.2 ± 3.0	111/115
40 ks	0.83 ± 0.23	1.68 ± 0.06	6.38 ± 0.03	7.5 ± 2.2	45^{+15}_{-10}	180^{+200}_{-20}	10.5 ± 5.0	-	-	< 1.6	104/114
45 ks	0.92 ± 0.22	1.68 ± 0.06	6.38 ± 0.04	8.7 ± 2.2	50^{+70}_{-30}	160^{+200}_{-160}	6.7 ± 4.3	-	-	< 1.6	104/113
50 ks	0.87 ± 0.19	1.66 ± 0.05	6.37 ± 0.03	7.6 ± 2.0	-	-	<4.6	-	-	< 2.6	115/114
55 ks	1.00 ± 0.21	1.66 ± 0.05	6.38 ± 0.03	9.8 ± 2.0	-	-	<4.4	-	-	< 3.2	127/114
60 ks	0.90 ± 0.19	1.69 ± 0.05	6.38 ± 0.05	6.3 ± 2.9	-	-	<8.5	140^{+30}_{-90}	30^{+60}_{-100}	2.8 ± 2.4	113/115
65 ks	0.91 ± 0.18	1.72 ± 0.05	6.38 ± 0.03	8.1 ± 2.4	-	-	<10.2	-	-	< 4.4	127/117
70 ks	0.90 ± 0.18	1.66 ± 0.05	6.39 ± 0.05	6.1 ± 2.3	-	-	<9.5	-	-	< 4.5	127/117
75 ks	0.95 ± 0.18	1.72 ± 0.05	6.41 ± 0.03	9.5 ± 2.5	-	-	<10.3	180^{+20}_{-170}	50^{+60}_{-15}	2.7 ± 2.3	123/111
80 ks	0.90 ± 0.20	1.66 ± 0.05	6.40 ± 0.03	9.0 ± 2.5	-	-	<5.3	-	-	<5.0	117/114
85 ks	0.81 ± 0.18	1.69 ± 0.05	6.38 ± 0.05	5.7 ± 2.4	40^{+10}_{-5}	175^{+155}_{-22}	12.0 ± 5.3	-	-	<2.5	127/114
90 ks	0.85 ± 0.18	1.68 ± 0.05	6.40 ± 0.07	5.3 ± 3.0	80^{+70}_{-35}	180^{+170}_{-20}	9.9 ± 5.0	-	-	<4.2	118/120
95 ks	0.90 ± 0.19	1.69 ± 0.06	6.41 ± 0.04	6.4 ± 2.1	-	-	<6.0	-	-	<2.7	100/119
100 ks	1.15 ± 0.20	1.74 ± 0.05	6.38 ± 0.03	8.1 ± 2.2	-	-	<7.7	-	-	<3.5	121/117
105 ks	0.94 ± 0.20	1.67 ± 0.06	6.38 ± 0.03	9.3 ± 2.3	-	-	<6.7	-	-	<4.4	121/116
110 ks	0.81 ± 0.20	1.67 ± 0.06	6.40 ± 0.03	8.4 ± 2.3	-	-	<11.5	-	-	<3.8	102/115
115 ks	0.77 ± 0.21	1.60 ± 0.06	6.39 ± 0.03	8.7 ± 2.3	-	-	<8.2	-	-	<4.0	114/114
120 ks	0.76 ± 0.20	1.62 ± 0.06	6.38 ± 0.04	6.0 ± 2.5	35^{+25}_{-15}	180^{+200}_{-20}	9.2 ± 5.6	150^{+50}_{-120}	60^{+70}_{-40}	2.8 ± 2.3	129/111
125 ks	0.80 ± 0.21	1.60 ± 0.06	6.38 ± 0.04	6.2 ± 2.5	30^{+5}_{-10}	180^{+300}_{-30}	9.4 ± 5.1	-	-	<4.2	132/114
130 ks	1.00 ± 0.20	1.71 ± 0.06	6.38 ± 0.04	6.2 ± 2.5	10^{+5}_{-3}	180^{+200}_{-20}	16.0 ± 8.4	-	-	< 2.9	124/114
Orbit 2											
177 ks	0.81 ± 0.23	$1.63^{+0.07}_{-0.06}$	6.40 ± 0.03	8.7 ± 2.0	-	-	<7.6	-	-	<1.2	108/110
182 ks	0.92 ± 0.21	1.64 ± 0.06	$6.38^{+0.04}_{-0.03}$	6.1 ± 2.0	-	-	<5.7	>150	30^{+100}_{-40}	2.6 ± 2.0	127/111
187 ks	$0.98^{+0.20}_{-0.32}$	$1.67^{+0.08}_{-0.09}$	$6.33^{+0.05}_{-0.03}$	7.3 ± 2.2	43^{+15}_{-22}	170^{+250}_{-40}	7.7 ± 4.5	> 45	70^{+50}_{-10}	7.7 ± 2.5	127/108
191 ks	0.86 ± 0.25	$1.63^{+0.06}_{-0.05}$	6.31 ± 0.05	5.0 ± 2.1	14^{+2}_{-7}	180^{+180}_{-15}	11.5 ± 4.7	> 400	100^{+240}_{-50}	4.7 ± 2.0	112/110
196 ks	0.78 ± 0.25	1.59 ± 0.06	6.37 ± 0.03	7.9 ± 1.8	-	-	<9.6	> 350	80^{+250}_{-25}	5.4 ± 2.2	94/112
202 ks	0.98 ± 0.20	1.65 ± 0.05	6.36 ± 0.03	$7.4^{+1.8}_{-2.0}$	28^{+10}_{-8}	120^{+280}_{-30}	8.4 ± 2.5	-	-	<2.5	130/111
208 ks	0.81 ± 0.20	1.59 ± 0.06	6.39 ± 0.05	7.6 ± 2.5	-	-	<6.9	-	-	<4.6	110/115
214 ks	1.03 ± 0.22	1.67 ± 0.07	6.37 ± 0.05	5.5 ± 2.5	70^{+70}_{-45}	180^{+250}_{-30}	6.2 ± 3.2	50^{+200}_{-35}	65^{+150}_{-25}	3.2 ± 2.7	85/109
220 ks	0.86 ± 0.22	1.57 ± 0.06	6.41 ± 0.03	7.5 ± 2.0	-	-	< 8.2	-	-	< 2.9	103/113
225 ks	1.02 ± 0.20	1.65 ± 0.05	6.35 ± 0.05	6.0 ± 2.0	18^{+5}_{-3}	160^{+190}_{-15}	11.6 ± 5.1	-	-	<2.3	107/127
231 ks	0.86 ± 0.21	1.62 ± 0.06	6.39 ± 0.04	7.1 ± 1.9	20^{+25}_{-15}	165^{+180}_{-20}	6.0 ± 4.8	-	-	<3.1	133/111
237 ks	0.73 ± 0.20	1.60 ± 0.06	6.41 ± 0.05	5.8 ± 2.4	-	-	<3.6	20^{+30}_{-5}	45^{+25}_{-15}	$6.1^{+3.0}_{-4.1}$	114/110
243 ks	0.89 ± 0.21	1.62 ± 0.06	6.38 ± 0.04	7.2 ± 2.3	-	-	<9.0	-	-	<6.0	142/113
249 ks	1.00 ± 0.21	1.65 ± 0.06	6.39 ± 0.03	7.3 ± 2.0	-	-	<9.5	> 50	60^{+180}_{-60}	2.6 ± 2.2	114/111
254 ks	0.80 ± 0.20	1.63 ± 0.07	6.39 ± 0.03	6.0 ± 2.0	30^{+15}_{-10}	130^{+220}_{-40}	4.8 ± 3.4	-	-	<3.6	98/113
260 ks	0.81 ± 0.19	1.59 ± 0.06	6.39 ± 0.03	8.8 ± 2.1	-	-	<9.0	-	-	<3.5	113/118
266 ks	0.78 ± 0.21	1.62 ± 0.06	6.36 ± 0.04	6.2 ± 2.0	17^{+8}_{-10}	160^{+180}_{-40}	6.2 ± 5.2	-	-	<2.5	117/112
272 ks	0.86 ± 0.21	1.61 ± 0.06	6.42 ± 0.04	8.9 ± 2.0	15^{+4}_{-6}	160^{+200}_{-15}	12.9 ± 5.8	-	-	<2.0	85/113
278 ks	0.80 ± 0.18	1.56 ± 0.06	6.40 ± 0.02	7.5 ± 2.0	-	-	<7.2	-	-	<2.5	106/116
283 ks	0.88 ± 0.20	1.68 ± 0.05	6.39 ± 0.03	9.0 ± 2.0	-	-	<7.2	-	-	<2.5	121/116
289 ks	0.73 ± 0.20	1.60 ± 0.05	6.38 ± 0.02	8.0 ± 2.0	-	-	<9.8	> 180	20^{+50}_{-80}	2.2 ± 2.0	119/111
295 ks	0.91 ± 0.20	1.60 ± 0.06	6.40 ± 0.03	8.0 ± 2.0	-	-	<8.8	-	-	<3.0	121/116
301 ks	0.89 ± 0.20	1.61 ± 0.06	6.36 ± 0.04	5.8 ± 2.1	-	-	<9.2	30^{+120}_{-15}	40^{+70}_{-10}	4.4 ± 3.2	87/112
304 ks	1.06 ± 0.30	1.68 ± 0.08	6.43 ± 0.05	6.9 ± 2.7	15^{+5}_{-5}	130^{+270}_{-40}	11.7 ± 8.0	> 200	50^{+100}_{-40}	3.2 ± 2.5	102/102

Table A1. Best fit parameters of the time-resolved XMM analysis. Column densities are in cm^{-2} units, energies are in keV units, normalizations are in $\text{ph cm}^{-2} \text{s}^{-1}$ units, r_{in} are in r_g units and ϕ are in degrees units. See Sect. 3.3.2 for details on the model.

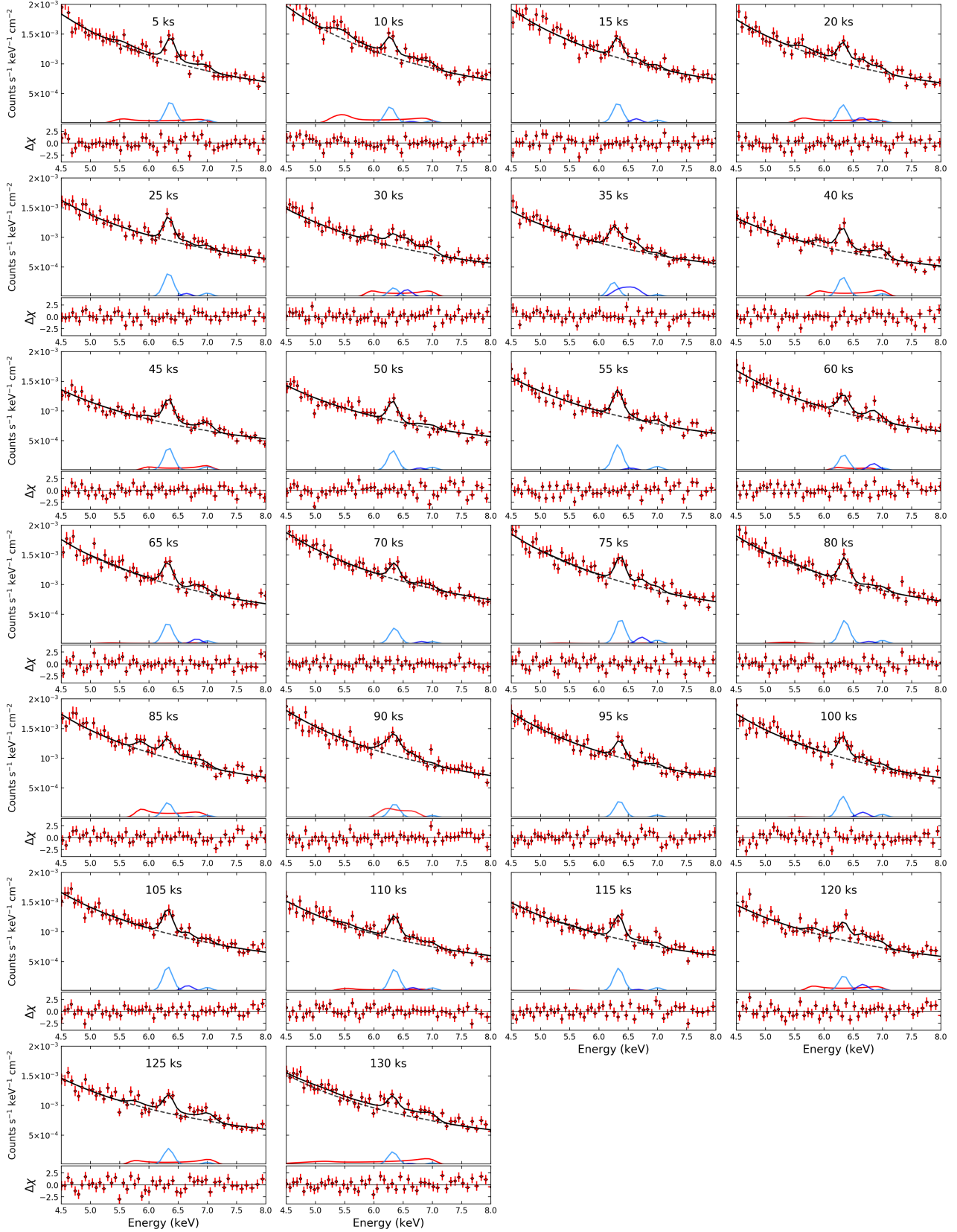


Figure A1. XMM EPIC pn data (divided by the instrumental effective area), best fits and residuals are shown, in the 4.5-8.0 keV band. Black solid lines indicate best fit models, dashed black lines indicate the power law spectral component, cyan solid lines indicate best fit iron $K\alpha$ and $K\beta$ components, red and blue solid lines indicate the two KYNRLINE components (*red flare* + *blue flare II* and *blue flare I*).

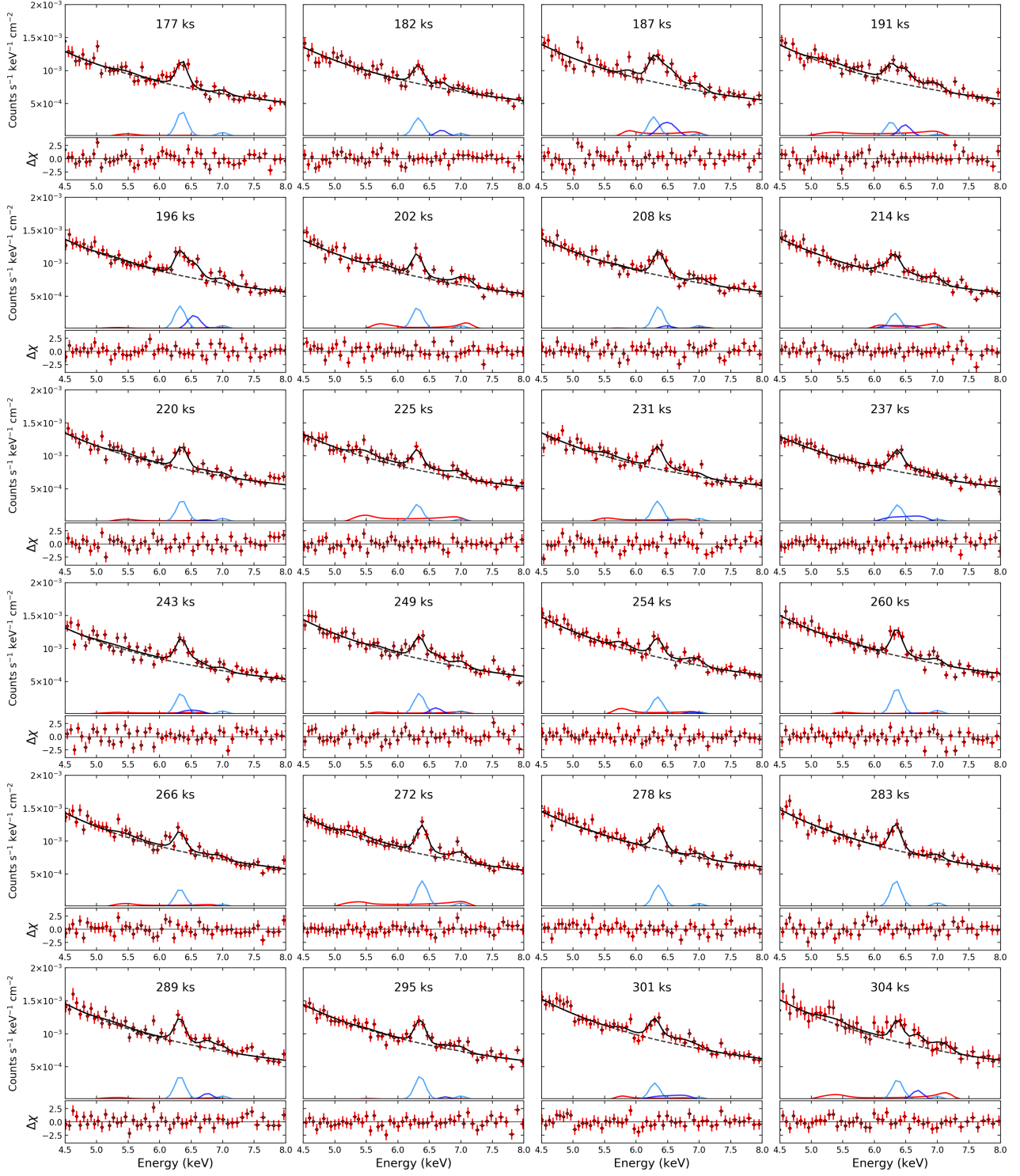


Figure A2. *continued.*